

# Diagnosis of ultrafast ultraintense laser pulse characteristics by machine-learning-assisted electron spin

Cite as: *Matter Radiat. Extremes* 8, 034401 (2023); doi: 10.1063/5.0140828

Submitted: 31 December 2022 • Accepted: 26 February 2023 •

Published Online: 21 March 2023








View Online



Export Citation



CrossMark

Zhi-Wei Lu,<sup>1</sup>  Xin-Di Hou,<sup>1</sup> Feng Wan,<sup>1,a)</sup>  Yousef I. Salamin,<sup>2</sup>  Chong Lv,<sup>3</sup> Bo Zhang,<sup>4</sup>  Fei Wang,<sup>5</sup>   
Zhong-Feng Xu,<sup>1</sup> and Jian-Xing Li<sup>1,b)</sup>

## AFFILIATIONS

<sup>1</sup>Ministry of Education Key Laboratory for Nonequilibrium Synthesis and Modulation of Condensed Matter, Shaanxi Province Key Laboratory of Quantum Information and Quantum Optoelectronic Devices, School of Physics, Xi'an Jiaotong University, Xi'an 710049, China

<sup>2</sup>Department of Physics, American University of Sharjah, P.O. Box 26666, Sharjah, United Arab Emirates

<sup>3</sup>Department of Nuclear Physics, China Institute of Atomic Energy, P.O. Box 275(7), Beijing 102413, China

<sup>4</sup>Key Laboratory of Plasma Physics, Research Center of Laser Fusion, China Academy of Engineering Physics, Mianshan Rd. 64#, Mianyang, Sichuan 621900, China

<sup>5</sup>School of Mathematics and Statistics, Xi'an Jiaotong University, Xi'an, Shaanxi 710049, China

<sup>a)</sup>Author to whom correspondence should be addressed: wanfeng@xjtu.edu.cn

<sup>b)</sup>Electronic mail: jianxing@xjtu.edu.cn

## ABSTRACT

The rapid development of ultrafast ultraintense laser technology continues to create opportunities for studying strong-field physics under extreme conditions. However, accurate determination of the spatial and temporal characteristics of a laser pulse is still a great challenge, especially when laser powers higher than hundreds of terawatts are involved. In this paper, by utilizing the radiative spin-flip effect, we find that the spin depolarization of an electron beam can be employed to diagnose characteristics of ultrafast ultraintense lasers with peak intensities around  $10^{20}$ – $10^{22}$  W/cm<sup>2</sup>. With three shots, our machine-learning-assisted model can predict, simultaneously, the pulse duration, peak intensity, and focal radius of a focused Gaussian ultrafast ultraintense laser (in principle, the profile can be arbitrary) with relative errors of 0.1%–10%. The underlying physics and an alternative diagnosis method (without the assistance of machine learning) are revealed by the asymptotic approximation of the final spin degree of polarization. Our proposed scheme exhibits robustness and detection accuracy with respect to fluctuations in the electron beam parameters. Accurate measurements of ultrafast ultraintense laser parameters will lead to much higher precision in, for example, laser nuclear physics investigations and laboratory astrophysics studies. Robust machine learning techniques may also find applications in more general strong-field physics scenarios.

© 2023 Author(s). All article content, except where otherwise noted, is licensed under a Creative Commons Attribution (CC BY) license (<http://creativecommons.org/licenses/by/4.0/>). <https://doi.org/10.1063/5.0140828>

## I. INTRODUCTION

Recent rapid advances in ultrafast ultraintense laser technology<sup>1,2</sup> have opened up broad prospects for vital investigations in laser–plasma physics,<sup>3–5</sup> laser nuclear physics,<sup>6,7</sup> laboratory astrophysics,<sup>8,9</sup> and particle physics.<sup>10,11</sup> In particular, laser systems with peak intensities in the hundreds of terawatt to multi-petawatt ranges have achieved laboratory intensities

of the order of  $10^{20}$ – $10^{22}$  W/cm<sup>2</sup>, recently even reaching  $\sim 10^{23}$  W/cm<sup>2</sup> with a pulse duration of tens of femtoseconds.<sup>12</sup> These achievements are paving the way for explorations of strong-field quantum electrodynamics (SF-QED), among other significant applications. Meanwhile, the unprecedented laser intensities not only cause large fluctuations in the laser output ( $\sim 1\%$ – $20\%$  in peak power<sup>12</sup>), but also make accurate determination of the laser parameters increasingly difficult. These parameters play key roles

throughout the laser-driven physical processes. For instance, in detection of the quantum radiation reaction effects, energy loss of the scattered electron beam serves as the SF-QED signal and is strongly correlated with the laser intensity and pulse duration.<sup>13,14</sup> In the fast ignition of inertial confinement fusion, specific and precise pulse duration and intensity ( $\sim 10^{20}$  W/cm<sup>2</sup>) of the ignition laser are required for improving the energy conversion from laser to fuel and suppressing uncertainties in the laser–plasma interactions.<sup>6,15</sup> In laser–plasma acceleration, the peak intensity and pulse duration affect the electron and proton acceleration efficiency and stability.<sup>16–18</sup> Uncertainties in the focal spot, pulse duration, and intensity of the laser pulse can lead to significant deviations from the parameters present in experiments. Thus, accurate determination of the spatiotemporal properties of ultrafast ultraintense laser pulses is a fundamental concern for today’s laser–matter interaction experiments.

Currently, laser spatiotemporal characteristics are diagnosed via separate measurements: for example, focal spot size via the high-resolution optical imaging technique<sup>12</sup> and temporal pulse duration via the frequency-resolved optical grating (FROG) technique.<sup>19</sup> Both of these techniques can reach an extremely high resolution, and their accuracy is limited only by the detector, experimental noise, or post-processing.<sup>19</sup> However, for high-power lasers, the pulse energy has to be reduced by several orders of magnitude to minimize damage to the optical instruments, with the results then being extrapolated to the case of full laser power.<sup>20–22</sup> Owing to nonlinear effects in the amplifying and focusing systems, the characteristics of a space–time coupled laser pulse obtained with these methods may deviate significantly from the exact values.<sup>23–25</sup> More reliable parameter diagnosis may be achieved via laser–matter interactions, making it possible to directly extract spatial and temporal information on ultrafast ultraintense ( $I_0 \gtrsim 10^{20}$  W/cm<sup>2</sup>) laser pulses. Three mainstream diagnostic approaches are currently in use. The first of these is atomic tunneling ionization, in which the nonlinear dependence of the multiple-tunneling-ionization rate on the field strength can be used to diagnose the laser peak intensity alone, with an accuracy of  $\lesssim 30\%$ – $50\%$ . However, the barrier suppression effect destroys the accuracy, and the atom species needs to be carefully chosen to match the laser intensity requirements.<sup>21,26,27</sup> Second, with vacuum acceleration of charged particles, the laser peak intensity, focal spot size, and pulse duration can be retrieved from particle spectral analysis. Here, though, the prepulse and plasma effects and the low statistics substantially influence the final spectra, and therefore one still needs more elaborate considerations.<sup>20,28–31</sup> Third, SF-QED effects can be used, for example, to predict the laser intensity and pulse duration separately via analysis of the spectra of electrons,<sup>32,33</sup> photons,<sup>22,34–36</sup> and positrons,<sup>37</sup> with a detection accuracy of  $\gtrsim 10\%$  for laser intensities within the range of  $10^{20}$ – $10^{23}$  W/cm<sup>2</sup>. Clearly, these methods either require separate diagnoses or can only measure low-precision laser parameter values (the maximum inaccuracy can reach  $\approx 50\%$ ). Thus, there remains an urgent need for new detection methods that can achieve high accuracy and simultaneously diagnose the laser intensity, pulse duration, and focal information.

Recent studies have indicated that the spin polarization of the electrons is sensitive to the field strength and profile of the intense laser pulse and thus can be manipulated by a laser pulse via the radiative spin-flip effect.<sup>38–40</sup> These findings have motivated us to

explore the possibilities of decoding the pulse information from the spin polarization of the laser-scattered electron beam.

In recent decades, machine learning (ML) techniques have come to be widely used in particle physics<sup>41</sup> and astrophysics,<sup>42</sup> and they are now having an increasing impact on the study of multiscale, highly nonlinear physical processes such as those arising in condensed matter physics and quantum materials science.<sup>43–45</sup> ML-assisted methods are more specialized than humans in comprehending multimodal data (acoustic, visual, and numerical) and optimizing nonlinear extreme physical systems<sup>46</sup> and thus can save much time and human effort when integrated into working practices.<sup>47,48</sup> In particular, data-driven methods are reshaping our exploration of extreme physical systems, such as in the interaction of ultrafast ultraintense lasers with materials.<sup>49</sup> The experimental realization of such extreme conditions in millimeter-sized plasmas can provide laboratory models of astrophysical scenarios.<sup>50</sup> The large quantities of data from such experiments or simulations need to be systematically managed. For instance, around 150 GB of data can be generated in each shot of the National Ignition Facility (NIF), and over 70 GB per minute in the Linac-Coherent-Light-Source (LCLS).<sup>51</sup> Handling data this size is becoming beyond the capabilities of conventional methods, with the consequence that the underlying physics of the phenomena under study may become obscured. By contrast, ML-assisted methods can be data-driven and run in parallel on large-scale central processing unit (CPU) or graphics processing unit (GPU) platforms to extract internal correlations between desired physical quantities.

In this paper, we propose an ML-assisted method to directly diagnose the spatiotemporal characteristics (peak intensity, focal spot size, and pulse duration) of a linearly polarized (LP) laser pulse, based on spin analysis of nonlinear Compton-scattered electron beams. The interaction scenario and framework of the ML algorithm are illustrated in Fig. 1. First, a high-energy transversely spin-polarized (TSP) electron beam is generated via laser-wakefield acceleration with polarization degree  $\bar{S}_i$ , mean energy  $\epsilon_i$ , and beam radius  $w_e$ ;<sup>52,53</sup> subsequently, this TSP electron beam is scattered by an ultrafast ultraintense LP laser (with peak intensity  $\xi$ , focal radius  $w_0$  and pulse duration  $\tau$ ) via nonlinear Compton scattering (NCS). Owing to the radiative spin-flip effect, the degree of

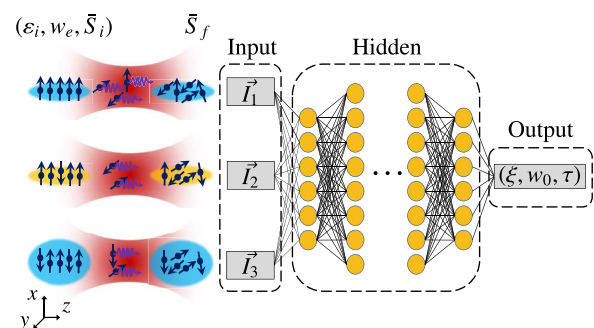


**FIG. 1.** Left: Three different electron beams propagating along the  $z$  direction with parameters  $\epsilon_i$ ,  $w_e$ , and  $\bar{S}_i$  scatter off the same laser pulse and produce final spin degrees of polarization  $\bar{S}_f$ . Right: Topology of the BPNN used for parameter prediction, which takes  $I_{j=1,2,3} = [\epsilon_i, w_e, \bar{S}_i, \bar{S}_f, \ln(\bar{S}_f/\bar{S}_i)]$  as input data and produces  $(\xi, w_0, \tau)$  as output; for details, see Sec. II B.

polarization changes from an initial  $\tilde{S}_i$  to a final  $\tilde{S}_f$ .<sup>38,54,55</sup> The difference (i.e., degree of depolarization)  $\delta\tilde{S} \equiv \tilde{S}_i - \tilde{S}_f$  will be the key factor for determining the laser pulse parameters. Finally, the initial and final electron beam parameters are encoded as a dataset  $\vec{I}_j$ , which is then used to train a neural-network ML algorithm and benchmark the training efficiency. Here,  $E_0$ ,  $\omega_0$ ,  $\xi \equiv eE_0/m\omega_0$ ,  $w_0$ , and  $\tau$  are the electric field strength, frequency, normalized intensity, focal radius, and pulse duration, respectively, of the LP laser pulse, and  $-e$  and  $m$  are the charge and mass, respectively, of the electron. Relativistic units with  $c = \hbar = 1$  will be used throughout. In addition, a one-to-one mapping between the beam parameters ( $\varepsilon_i, w_e, \tilde{S}_i, \tilde{S}_f$ ) and the laser parameters ( $\xi, w_0, \tau$ ) can be a formidable task, because only one output is of relevance, namely,  $\tilde{S}_f$ . To determine the three unknown laser parameters ( $\xi, w_0, \tau$ ) simultaneously, at least three sets of output values of  $\tilde{S}_f$  are required. Therefore, three independent beams with different parameter combinations are employed here. These complex multidimensional relationships can be effectively handled by the neural network topology shown in Fig. 1. Note that this method can induce a spin depolarization of  $\approx 30\%$  for 1 GeV electrons, and  $\approx 40\%$  for 2 GeV ones (laser parameters  $\xi \approx 80$  and  $\tau = 14T_0$ ). Currently available spin polarimetries for electrons are based on Mott scattering,<sup>56</sup> Møller scattering,<sup>57</sup> linear Compton scattering,<sup>58</sup> or more efficient NCS.<sup>59</sup> Some recent studies have indicated that the detection precision of NCS-based polarimetry can reach about 0.3%,<sup>59</sup> which qualifies the spin-based method as a new type of high-accuracy diagnostic scheme for ultrafast ultraintense laser pulses.

In Sec. II, a brief description of the Monte Carlo (MC) simulation method of spin-resolved NCS is given, together with the simulation parameters. This is followed by an introduction to our laser-parameter retrieval technique based on ML algorithms (see Fig. 1) and the associated asymptotic formulas. Numerical results and a brief discussion are given in Sec. III. Our conclusions are presented in Sec. IV.

## II. SPIN-BASED LASER-PARAMETER DIAGNOSTIC METHODS

As an illustrative example, diagnosis of a tightly focused laser with a double-Gaussian (spatial and temporal) distribution is considered. In principle, the envelope of the laser can be arbitrary, but should be predetermined via experimental methods, for instance, from a low-power splitting beam. Once the envelope form is known, the following methods can be used to retrieve the laser pulse parameters from the spin diagnosis of the scattered electrons.

### A. Spin-resolved NCS and interaction scenario

Our analysis of the radiative spin-flip effect is based on the MC simulation method proposed in Refs. 38 and 60, in which the spin-resolved probability of NCS in the laser-beam scattering is considered in the local constant field approximation (LCFA).<sup>38,61</sup> After emission of a photon, the electron spin state collapses into one of its basis states defined with respect to an instantaneous spin quantization axis (SQA) chosen along the magnetic field in the rest frame of the electron. In Fig. 1, the laser is linearly polarized along the  $x$  direction, and so its magnetic field component is  $B_y$ . The SQA tends to be antiparallel to the magnetic field in the rest frame of the electron. Depolarization amounts to the electron spin

acquiring a certain spin polarization in the  $y$  direction, which is canceled from the net polarization by the periodic magnetic field, i.e.,  $\tilde{S}_{f,y} \approx 0$ . Therefore, we focus our analysis in what follows on the electron polarization in the  $x$  direction. In NCS, the invariant parameter characterizing the quantum effects is<sup>61,62</sup>  $\chi \equiv e\sqrt{-(F_{\mu\nu}p^\nu)^2}/m^3$ , where  $F_{\mu\nu}$  and  $p^\nu$  denote the electromagnetic field tensor and the four-momentum of the electron, respectively. In a colliding geometry,  $\chi \approx 2\xi\gamma_e\omega_0/m$ , where  $\gamma_e$  denotes the electron's Lorentz factor. To excite the radiative spin-flip process,  $\chi$  should be in the range of 0.01–1, over which nonlinear Breit–Wheeler pair production can be suppressed.

The LP laser parameter set for the training data includes wavelength  $\lambda_0 = 0.8 \mu\text{m}$ , focal radius  $w_0 = [2, 3, 4, 5]\lambda_0$ , peak intensity  $\xi = [10, 15, 20, 30, 40, 45, 60, 80]$ , and pulse duration  $\tau = [2, 6, 10, 14]T_0$ , with  $T_0$  denoting the laser period. The probe electron beam has a polar angle  $\theta_e = \pi$ , azimuthal angle  $\phi_e = 0$ , and angular divergence  $\sigma_\theta = 0.3 \text{ mrad}$ . The initial kinetic energies are  $\varepsilon_i = [0.5, 1, 1.5, 2] \text{ GeV}$ , with relative energy spread  $\sigma_\varepsilon/\varepsilon_i = 0.05$ , and the initial average degree of spin polarization along the  $x$  direction  $\tilde{S}_{i,x} = [0.6, 0.8, 1.0]$  (here,  $\chi_{\text{max}} \lesssim 1$ , i.e., the pair-production effect on the final electron distribution is negligible for the present parameters). The beam radius  $w_e = [1, 2, 3, 4]\lambda_0$ , the beam length  $L_e = 5\lambda_0$ , and the total number of electrons is  $5 \times 10^5$  with transversely Gaussian and longitudinally uniform distributions, attainable by current laser wakefield accelerators.<sup>3</sup>

### B. Neural network assisted diagnosis

Decoding the spatiotemporal characteristics of an ultrafast ultraintense laser from information carried by a scattered electron beam is an inverse transformation that requires multidimensional input and output. In principle, the equation of motion can be embedded in the neural network, which can predict one laser parameter with high accuracy. However, predicting three laser parameters simultaneously will be inefficient owing to slow real-time integration of the equation of motion. Here, therefore, a data-driven standard backpropagation neural network (BPNN) based on the PyTorch framework is used to train and predict the scattering laser parameters.<sup>63</sup> The input data are composed of the energy, beam radius, the initial and final average spins, and the logarithm of the ratio of final spin to initial spin of the electron beam, in the vector  $\vec{I} \equiv [\varepsilon_i, w_e, \tilde{S}_i, \tilde{S}_f, \ln(\tilde{S}_f/\tilde{S}_i)]$ ; see Fig. 1. About 1000 sets of input data are obtained via the MC simulation and rearranged/recombined to about  $3 \times 10^4$  sets for training. Then the input data ( $\vec{I}_1, \vec{I}_2, \vec{I}_3$ ) are normalized via the `StandScaler` function. After random permutation, the input information is preprocessed by the second-order polynomial feature function `PolynomialFeatures` to construct implicit connections between them.

In our BPNN, we choose eight fully connected hidden layers, with 128, 256, 512, 512, 512, 512, 256, and 128 nodes respectively. The numbers of hidden layers and nodes here ensure adequate prediction accuracy and appropriate computing resources. The activation functions use `tanh` and `ReLU` alternatively between different layers. The mean squared error `MSELoss` is used as the loss function, and the stochastic gradient descent `SGD` method is used as the optimizer. After each training iteration, the optimizer clears old gradients, and losses are backpropagated for the calculation of new gradients. Finally, the network parameters are updated according

to the new gradients. The initial learning rate is set as 0.3, and the adjustment factor of the exponential learning rate ExponentialLR scheduler is set as 0.9. In our calculations, the total number of training iterations is  $4 \times 10^4$ . To enhance the learning efficiency of the model on the laser pulse duration  $\tau$ , we consider two models with learning ratios of  $\xi$ ,  $w_0$ , and  $\tau$  set as 1:1:1 and 1:1:2, respectively [see Figs. 2(a) and 2(b)]. Note that the training loss measures the training efficiency of the model. The training loss may increase as a result of inappropriate network structure design and will decrease with effective learning. In the final stable stage, there may be overfitting to the training data. However, the overfitting can be restrained by using a technique such as weight upper limit<sup>64</sup> or dropout.<sup>65</sup> For instance, the losses of  $\xi$ ,  $w_0$ , and  $\tau$  are reduced for the learning ratio of 1:1:2, and further increasing the ratio of  $\tau$  will produce larger losses in other parameters. This BPNN model will be used in the subsequent prediction. In principle, the ML-assisted method is not limited to the current application, but can also be used for other inverse problems.

### C. Analytical asymptotic models

Asymptotic estimation of the depolarization effect is done below analytically from the radiative equations of motion for the dynamics [the Landau–Lifshitz (LL) equation<sup>66</sup>] and the spin [the modified Thomas–Bargmann–Michel–Telegdi (T-BMT) equation<sup>67</sup>]. A dependence of the spin dynamics on the electron energy follows, assuming weak radiation. The quantum-corrected LL equation is then used to obtain the approximate electron energy, which is then plugged into the solution for spin dynamics.

The radiative spin evolution is composed of Thomas precession (subscript  $T$ ) and radiative correction (subscript  $R$ ) terms<sup>67</sup> and is governed by

$$\begin{aligned} \frac{d\mathbf{S}}{d\eta} &= \left( \frac{d\mathbf{S}}{d\eta} \right)_T + \left( \frac{d\mathbf{S}}{d\eta} \right)_R, \quad (1a) \\ \left( \frac{d\mathbf{S}}{d\eta} \right)_T &= \frac{e\gamma_e}{(k \cdot p_i)} \mathbf{S} \times \left[ -\left( \frac{g}{2} - 1 \right) \frac{\gamma_e}{\gamma_e + 1} (\boldsymbol{\beta} \cdot \mathbf{B}) \boldsymbol{\beta} \right. \\ &\quad \left. + \left( \frac{g}{2} - 1 + \frac{1}{\gamma_e} \right) \mathbf{B} - \left( \frac{g}{2} - \frac{\gamma_e}{\gamma_e + 1} \right) \boldsymbol{\beta} \times \mathbf{E} \right], \quad (1b) \end{aligned}$$

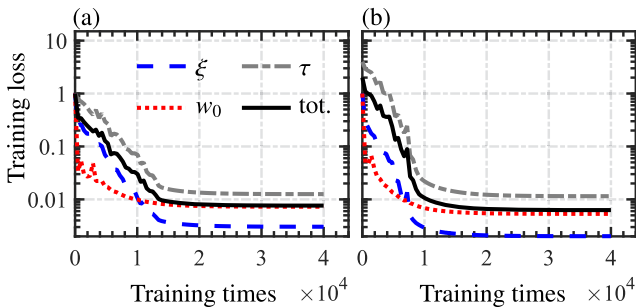


**FIG. 2.** Training loss (mean squared errors for all training samples) evolutions of  $\xi$ ,  $w_0$ ,  $\tau$ , and total loss (tot.) vs training time. Learning ratios of  $\xi$ ,  $w_0$  and  $\tau$  are 1:1:1 in (a) and 1:1:2 in (b).

$$\left( \frac{d\mathbf{S}}{d\eta} \right)_R = -P[\psi_1(\chi)\mathbf{S} + \psi_2(\chi)(\mathbf{S} \cdot \boldsymbol{\beta})\boldsymbol{\beta} + \psi_3(\chi)\mathbf{n}_B]. \quad (1c)$$

Here,  $\mathbf{E}$  and  $\mathbf{B}$  are the laser electric and magnetic fields, respectively;  $p_i$ ,  $k$ ,  $\eta$ , and  $g$  are the electron momentum 4-vector, the laser wavevector, the laser phase, and the electron gyromagnetic ratio, respectively; and

$$\begin{aligned} P &= \frac{\alpha_f m^2}{\sqrt{3} \pi (k \cdot p_i)}, \\ \psi_1(\chi) &= \int_0^\infty u'' du K_{2/3}(u'), \\ \psi_2(\chi) &= \int_0^\infty u'' du \int_{u'}^\infty dx K_{1/3}(x) - \psi_1(\chi), \\ \psi_3(\chi) &= \int_0^\infty u'' du K_{1/3}(u'), \\ u' &= \frac{2u}{3\chi}, \quad u'' = \frac{u^2}{(1+u)^3}, \quad u = \frac{\varepsilon_y}{\varepsilon_0 - \varepsilon_y}, \end{aligned}$$

where  $\varepsilon_0$  and  $\varepsilon_y$  are the electron energy before radiation and the emitted photon energy, respectively,  $K_n$  is the  $n$ th-order modified Bessel function of the second kind, and  $\alpha_f = 1/137$  is the fine structure constant. The SQA is chosen along the magnetic field  $\mathbf{n}_B = \boldsymbol{\beta} \times \hat{\mathbf{a}}$ , with  $\boldsymbol{\beta} = \mathbf{v}/c$  the scaled electron velocity and  $\hat{\mathbf{a}} = \mathbf{a}/|\mathbf{a}|$  the unit vector along the electron acceleration  $\mathbf{a}$ .

To facilitate theoretical analysis and extract analytical formulas, some approximations will be made with the current laser and electron beam parameters in mind, i.e., a GeV electron beam interacting with an LP laser ( $\xi < 100$ ) and  $0.1 \lesssim \chi \lesssim 1$ . Owing to laser defocusing, the Thomas-term-induced variation  $\delta S_T$  is  $\lesssim 10^{-4}$ , and only the dominant term, i.e., the radiative correction, will be considered. Furthermore, the initial velocity of the electron beam is along the  $z$  direction, with  $\beta_z \gg \beta_x(\beta_y)$ , and thus the  $\psi_2$  term is negligible for initially TSP electrons. Moreover, owing to the periodic nature of the magnetic field, the contribution of the  $\psi_3$  term vanishes on average within one laser period. Hence, the approximate evolution of the spin components may be obtained from

$$\frac{dS_x}{d\eta} \simeq \frac{C\psi_1(\chi)}{\gamma_e} S_x, \quad (2a)$$

$$\frac{dS_y}{d\eta} \simeq \frac{C\psi_1(\chi)}{\gamma_e} S_y, \quad (2b)$$

$$\frac{dS_z}{d\eta} \simeq \frac{C(\psi_1(\chi) + \psi_2(\chi))}{\gamma_e} S_z, \quad (2c)$$

where

$$C = -\frac{\alpha_f \omega_0}{2\sqrt{3}\pi m}.$$

Because  $\psi_1(\chi) > 0$  and  $\psi_2(\chi) < 0$ , depolarization in the  $x$  and  $y$  directions is faster than in the  $z$  direction. For instance, for a laser with parameters  $\xi = 60$ ,  $\tau = 8T_0$ , and  $w_0 = 5\lambda_0$ , and the electron beam of Fig. 4(a), the final average spin degrees of polarization are



$S_{x,f} \approx 0.8201$ ,  $S_{y,f} \approx 0.8211$ , and  $S_{z,f} \approx 0.8741$ , for  $\bar{S}_{i,x} = 1$ ,  $\bar{S}_{i,y} = 1$ , and  $\bar{S}_{i,z} = 1$ . Thus, in this paper, we take the electron beam to be initially polarized along the  $x$  direction for a larger detection signal.

Under the assumption of weak radiation loss, for which

$$\frac{dy_e}{d\eta} \simeq 0, \quad \chi(\eta) \simeq 2 \frac{\omega_0}{m} \gamma_e \xi \sin^2 \eta,$$

one can obtain, to the leading-order approximation,  $\psi_1(\chi) \simeq f_1 \chi^2$  for  $0.1 \lesssim \chi \lesssim 1$ , and  $f_1 \approx 0.25$  is obtained by curve fitting. Integrating Eq. (2a), the asymptotic  $\bar{S}_{f,x}$ , using the laser-beam parameters, will be given by

$$\ln \left[ \frac{\bar{S}_{f,x}(\tau)}{\bar{S}_{f,x}(0)} \right] \simeq M_1 \gamma_e \xi^2 \tau, \quad (3)$$

where the factor

$$M_1 = -\frac{\sqrt{3}}{2} \alpha_f \frac{\omega_0}{m} f_1 \approx -4.81 \times 10^{-9}$$

and  $\tau$  is the pulse duration in units of the laser period  $T_0$ .

To be precise, the radiated photon energy (radiation loss  $\bar{\varepsilon}_y$ ) should be taken into account for  $0.1 \lesssim \chi \lesssim 1$ . Here, we use the quantum-corrected LL equation to include the radiation loss<sup>68</sup> via

$$\frac{d\mathbf{p}}{dt} = \mathbf{F}_L + \mathbf{F}_{\text{rad}}, \quad (4a)$$

$$\mathbf{F}_{\text{rad}} = -C' \chi^2 \mathcal{G}(\chi) \boldsymbol{\beta} / |\boldsymbol{\beta}|^2, \quad (4b)$$

where  $\mathbf{F}_L \equiv q(\mathbf{E} + \boldsymbol{\nu} \times \mathbf{B})$  is the Lorentz force,  $\mathbf{F}_{\text{rad}}$  is the radiation reaction force,  $C' = 2\alpha_f^2 m/3r_e$  (with  $r_e$  the classical electron radius), and  $\mathcal{G}(\chi) \simeq [1 + 4.8(1 + \chi) \ln(1 + 1.7\chi) + 2.44\chi^2]^{-2/3}$  is the quantum correction function.<sup>69</sup> For  $0.1 \lesssim \chi \lesssim 1$ , assuming  $\chi(\eta) \simeq (2\omega_0/m) \gamma_e \xi \sin^2 \eta$  and making the approximation  $\chi^2 \mathcal{G}(\chi) \simeq f_2 \chi^2$  (with a fitting factor of  $f_2 \approx 0.077$ ), the radiation loss (averaged over all electrons, i.e., ignoring the stochastic effect) is given by

$$\bar{\varepsilon}_y = \int_0^\eta d\eta \mathbf{F}_{\text{rad}} \frac{dt}{d\eta} \simeq M_2 \tau \gamma_e^2 \xi^2,$$

where  $M_2 = (\pi \alpha_f \omega_0 / m) f_2 \approx 5.36 \times 10^{-9}$ . Then, replacing  $\gamma_e$  in Eq. (3) by  $\gamma_e - \bar{\varepsilon}_y$ , an analytical asymptotic estimate of the final spin  $\bar{S}_{f,x}$  is given by

$$\ln \left[ \frac{\bar{S}_{f,x}(\tau)}{\bar{S}_{f,x}(0)} \right] \simeq M_1 \gamma_e \xi^2 \tau (1 - M_2 \gamma_e \xi^2 \tau). \quad (5)$$

### III. RESULTS AND DISCUSSION

To demonstrate the efficiency of the proposed diagnostic method, some operational parameters of petawatt-scale lasers at a number of international facilities will be used; see Table I. The corresponding depolarization processes, investigated via MC simulations, indicate that the relative errors between the predicted and input parameters are of orders 0.1%–10%; see Fig. 3(a). After consecutive training, the BPNN model grasps the pattern of the radiative

**TABLE I.** Operational parameters of some international ultrafast ultraintense laser facilities: total energy  $E_L$ , central wavelength  $\lambda$ , peak intensity  $I_0$ , pulse duration  $\tau$ , and focal radius  $w_0$ .

Project	$E_L$ (J)	$\lambda$ ( $\mu\text{m}$ )	$I_0$ ( $\text{W}/\text{cm}^2$ ); $\xi$	$\tau$ (fs); $T_0$	$w_0$ ( $\lambda$ )
ELI-NP <sup>70</sup>	20	0.82	$5.6 \times 10^{21}$ ; 52.43	18.75; 6.86	3.63
J-KAREN <sup>71</sup>	28.4	0.8	$3.8 \times 10^{21}$ ; 42.14	32.9; 12.33	4.75
GIST <sup>72</sup>	44.5	0.81	$10^{22}$ ; 69.21	30; 11.1	3.79
SILEX-II <sup>73</sup>	30	0.8	$5 \times 10^{20}$ ; 15.28	30; 11.24	6.16
APOLLON <sup>74</sup>	10	0.815	$2 \times 10^{21}$ ; 31.14	24; 8.83	2.92

spin-flip effect and is therefore capable of accurately predicting the laser characteristics, i.e.,  $(\xi, \tau, w_0)$ , simultaneously. Owing to the limited weighting parameters and training data, the relative prediction errors for  $\xi$ ,  $\tau$ , and  $w_0$  (simultaneously) are of the order of  $\mathcal{R}_{1(2)} \lesssim 10\%$ ; see Figs. 3(b) and 3(c). Compared with cases with  $w_0 \gtrsim 3\lambda_0$ , the number of electrons scattered by a tightly focused laser ( $w_0 \lesssim 3\lambda_0$ ) is lower, owing to the small Rayleigh range ( $z_R = \pi w_0^2 / \lambda$ ). Thus, the beam-averaged spin-flip effect is relatively more sensitive to variations in the electron beam parameters, and the relative error  $\mathcal{R}_1$  is larger for  $w_0 \lesssim 3\lambda_0$  [see Fig. 3(b)]. For a laser radius  $w_0 \gtrsim 5\lambda_0$ , which is already beyond the current training range, a certain amount of overfitting is expected. For SILEX-II, for example, the relative

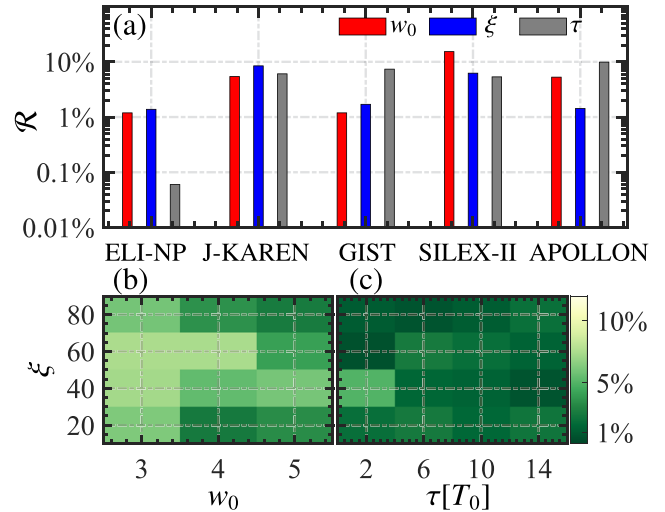


**FIG. 3.** (a) Relative errors  $\mathcal{R} = (\mathcal{R}_\xi, \mathcal{R}_\tau, \mathcal{R}_w)$  between predicted and theoretical values of  $(\xi, \tau, w_0)$  for the facilities in Table I, where  $\vec{l}_1$ ,  $\vec{l}_2$ , and  $\vec{l}_3$  are respectively  $(\varepsilon_i = 1 \text{ GeV}, w_e = \lambda_0, \bar{S}_{i,x} = 1)$ ,  $(\varepsilon_i = 1 \text{ GeV}, w_e = 3\lambda_0, \bar{S}_{i,x} = 1)$ , and  $(\varepsilon_i = 1.5 \text{ GeV}, w_e = \lambda_0, \bar{S}_{i,x} = 1)$ . (b) Distribution of total relative error  $\mathcal{R}_1 = \sqrt{\mathcal{R}_\xi^2 + \mathcal{R}_w^2}$  in the  $\xi$ - $w_0$  plane, where  $\tau = 10T_0$  and  $(\vec{l}_1, \vec{l}_2, \vec{l}_3)$  are the same as in (a). (c) Distribution of total relative error  $\mathcal{R}_2 = \sqrt{\mathcal{R}_\xi^2 + \mathcal{R}_\tau^2}$  in the  $\xi$ - $\tau$  plane, where  $w_0 = 5\lambda_0$ , and  $\vec{l}_1$ ,  $\vec{l}_2$ , and  $\vec{l}_3$  are respectively  $(\varepsilon_i = 500 \text{ MeV}, w_e = \lambda_0, \bar{S}_{i,x} = 1)$ ,  $(\varepsilon_i = 500 \text{ MeV}, w_e = 4\lambda_0, \bar{S}_{i,x} = 0.8)$ , and  $(\varepsilon_i = 2 \text{ GeV}, w_e = \lambda_0, \bar{S}_{i,x} = 0.6)$ .

error in the focal radius  $\mathcal{R}_w \sim 15\%$ . Moreover, for a specific  $\xi$ , the electron energy will damp rapidly within a certain  $\tau$ , and the depolarization will saturate owing to the much smaller  $\chi \ll 1$ . From the aspect of the ML algorithm, there might occur a sharp gradient along the pulse duration. As a consequence, for long pulse duration  $\tau$ , the complete prediction will be inaccurate and the growth in the relative errors will be quite rapid (owing to the limited training datasets). For instance, the relative errors in the cases of J-KAREN and SILEX-II are relatively large in Fig. 3(a), and similar trends can also be found in Fig. 3(c). In addition, as another key parameter for the NCS, once the peak intensity  $\xi$  is too small (i.e., when  $\chi$  will also be too small via  $\chi \propto \gamma_e \xi$ ), the statistical error in the MC calculation will increase and the prediction will be inaccurate, too. For instance, the relative errors for SILEX-II and APOLLON are larger than that of ELI-NP; see Fig. 3(a) and the general trends in Fig. 3(c). Therefore, for short pulse duration  $\tau$  and large intensity  $\xi$ , the relative errors will be lower than those in other cases, for instance, in the upper-left region of Fig. 3(c),  $\mathcal{R}$  can reach the order of  $\lesssim 0.1\%$ . It can be foreseen that with a larger network size, i.e., more weighting parameters, the model will be more accurate and robust.

The physical essence of the ML-assisted pulse information decoding method is revealed by our analytical asymptotic estimation on the basis of Eq. (5), which is in good agreement with the numerical MC results over a wide range of laser parameter values; see

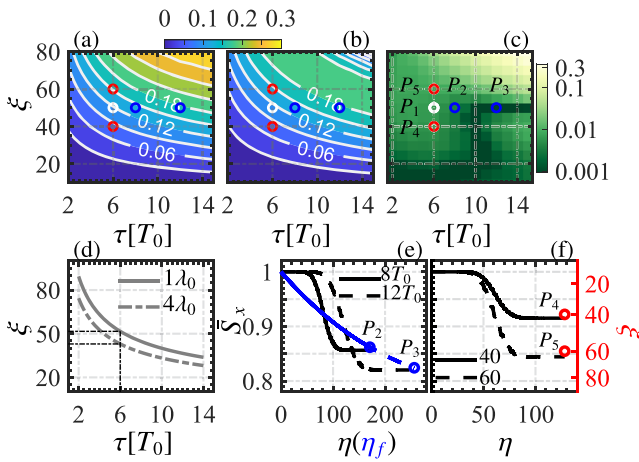


**FIG. 4.** (a) and (b) Transverse spin degrees of depolarization of the probe electron beams  $\delta\tilde{S}_x \equiv \tilde{S}_{i,x} - \tilde{S}_{f,x}$  vs laser peak intensity  $\xi$  and pulse duration  $\tau$ : (a)  $\delta\tilde{S}_x^{MC}$  calculated by the MC method; (b)  $\delta\tilde{S}_x^{AE}$  calculated by asymptotic estimation from Eq. (5). Here, a laser radius  $w_0 = 5\lambda_0$ , a probe electron beam energy  $\varepsilon_i = 1$  GeV, a beam radius  $w_e = \lambda_0$ , and an initial average spin  $\tilde{S}_{i,x} = 1$  are used. Other parameters are the same as in Fig. 3. (c) Relative error  $\mathcal{R}_s = |\delta\tilde{S}_x^{MC} - \delta\tilde{S}_x^{AE}| / \delta\tilde{S}_x^{MC}$  vs  $\xi$  and  $\tau$ . (d)  $\delta S(\xi, \tau) = 0.12$  [white circles  $P_1$  ( $\xi = 50$ ,  $\tau = 6T_0$ ) in (a)–(c)] for  $w_e = 1\lambda_0$  (solid line) and  $w_e = 4\lambda_0$  (dash-dotted line). (e)  $\tilde{S}_x$  vs laser phase  $\eta \equiv \omega_0(t - z)$ . The solid and dashed black lines (averaged MC evolution process) correspond to the blue circles  $P_2$  ( $\xi = 50$ ,  $\tau = 8T_0$ ) and  $P_3$  ( $\xi = 50$ ,  $\tau = 12T_0$ ) in (a)–(c), respectively. The blue lines and circles indicate the analytical calculations (only related to the final laser phase  $\eta_f$ ). (f)  $\tilde{S}_x$  vs laser phase  $\eta$ . The solid and dashed lines correspond to the red circles  $P_4$  ( $\xi = 40$ ,  $\tau = 6T_0$ ) and  $P_5$  ( $\xi = 60$ ,  $\tau = 6T_0$ ) in (a)–(c), respectively. Black lines are from the averaged MC evolution calculation and red circles (right axis) are from the analytical calculations.

Figs. 4(a)–4(c). The distributions of  $\delta\tilde{S}_x^{MC,AE}$  with respect to  $\xi$  and  $\tau$  are shown in Figs. 4(a) and 4(b), where superscripts “MC” and “AE” denote the results from the MC and analytical asymptotic estimation (AE) methods, respectively. As expected,  $\delta\tilde{S}_x$  increases as  $\xi$  and  $\tau$  both increase, and a specific spin change  $\delta\tilde{S}_x$  determines a curve that binds  $\xi$  with  $\tau$  (or a hyperplane for  $\xi$ ,  $\tau$ , and  $w_0$ ), i.e., the NCS acts as a nonlinear function  $\mathcal{F}(\cdot, \cdot)$  that maps the laser pulse parameters  $(\xi, \tau)$  to the degree of depolarization of the electron beam  $\mathcal{F}(\xi, \tau) \rightarrow \delta\tilde{S}_x$ . Quite remarkably, the corresponding relative error  $\mathcal{R}_s$  in the parameter ranges of  $\xi \in (10, 60)$  or  $\tau \in (2, 6)T_0$  is  $\mathcal{R}_s \approx 1\%$ ; see Fig. 4(c). With the analytical AE extracted subject to the condition  $0.1 < \chi \lesssim 1$ , and for  $\xi > 60$  and  $\tau > 6$ , the low-order estimation deviates from the MC result, owing to the nonlinear radiative effects. By contrast, the ML-assisted method is data-driven, i.e., the algorithms can still grasp the correlations between laser pulse parameters and depolarization of the electron beam, without artificial restrictions; see the prediction accuracy (the total relative error  $\mathcal{R}_2 \sim 1\%$ ) for high laser intensity and long pulse duration in Fig. 3(c).

Figure 4(d) illustrates how to determine  $\xi$  and  $w_0$  via AE for a specific set of parameters ( $\xi = 50$ ,  $\tau = 6T_0$ , and  $w_0 = 5\lambda_0$ ) marked as white circles  $P_1$  in Figs. 4(a)–4(c). Here, the pulse duration  $\tau$  is pre-acquired with other diagnostics, for instance, from the low-power mode of detection. Then, a sub-micrometer probe is collided with the laser pulse, from which one obtains  $\delta\tilde{S}_1$ ; see the solid line labeled “ $1\lambda_0$ ” in Fig. 4(d), which has been obtained from Eq. (5). After that, a second probe with beam radius  $w_e = 4\lambda_0$  produces  $\delta\tilde{S}_2$ , the dot-dashed line labeled “ $4\lambda_0$ ” in Fig. 4(d). According to Eq. (5), two average intensities  $\xi_1$  and  $\xi_2$  can be determined from  $\delta\tilde{S}_1$  and  $\delta\tilde{S}_2$ , respectively, corresponding to different beam radii. Since  $w_0 \gg w_e$ , the average laser intensity sensed by the sub-micrometer probe can serve approximately as the peak intensity in the focusing region. Thus,  $\xi_1 = 51.62$  is identified as the peak intensity of the laser pulse, with a relative error of 3.2%, whereas  $\xi_2 = 42.96$ , corresponding to  $w_e = 4\lambda_0$ , is taken as the average intensity within the probe radius, i.e.,  $\xi_2 = \xi_1 \int_{-w_e}^{w_e} \exp(-r^2/w_0^2) dr$ . Numerical calculation gives the focal radius  $w_0 = 5.18\lambda_0$ , with a relative error of 3.6%. Note that in Eq. (5), once  $\tau$  (or  $\xi$ ) is given, the map between  $\delta\tilde{S}$  and the other parameter is uniquely fixed. For instance, in Fig. 4(e), once  $\xi$  is fixed [points  $P_2$  and  $P_3$  in Figs. 4(a)–4(c)], there will be only one intersection (the final phase  $\eta_f$ ) between Eq. (5) and the temporal evolution of the average spin. Here,  $\tilde{S}(\eta_f)$  is the final degree of polarization of the electron beam. Conversely, once  $\tau$  is fixed [points  $P_4$  and  $P_5$  in Figs. 4(a)–4(c)], the MC final results will evolve to a unique  $\xi$  value; see Fig. 4(f).

Compared with the signals from dynamical statistics, the degree of spin polarization is more accurate and more robust with respect to fluctuations in energy and angular spread of the electron beam probe; see Figs. 5(a)–5(d). As the initial energy spread  $\sigma_\varepsilon/\varepsilon_i$  varies from 1% to 30%, the average energy ( $\bar{\varepsilon}_f \sim 500$  MeV) of the final electron beam ( $w_e = 1\lambda_0$ ,  $\varepsilon_i = 1$  GeV) changes by  $\sim 1\%$ ; see Fig. 5(a). However, the effect of energy spread on the spin polarization  $\tilde{S}_{f,x}$  of the final state is  $\sim 0.3\%$ ; see Fig. 5(c). According to Eq. (5) expressing the analytical AE,  $S_f \sim \exp(-k_1\gamma_e)$  and  $\delta S_f \sim \delta\gamma_e k_1 \exp(-k_1\gamma_e)$ , which leads to the conclusion that the spin variations due to dynamics exhibit exponential decay. Similarly, while the initial angular spread  $\sigma_\theta$  changes from 0.3 to 100 mrad, the normalized variation of angular spread  $N_\theta$  is  $\sim 30\%$ , and the effect on the spin  $\tilde{S}_{f,x}$  is  $\sim 0.2\%$ . In short, the detection accuracy of the spin signal is one to

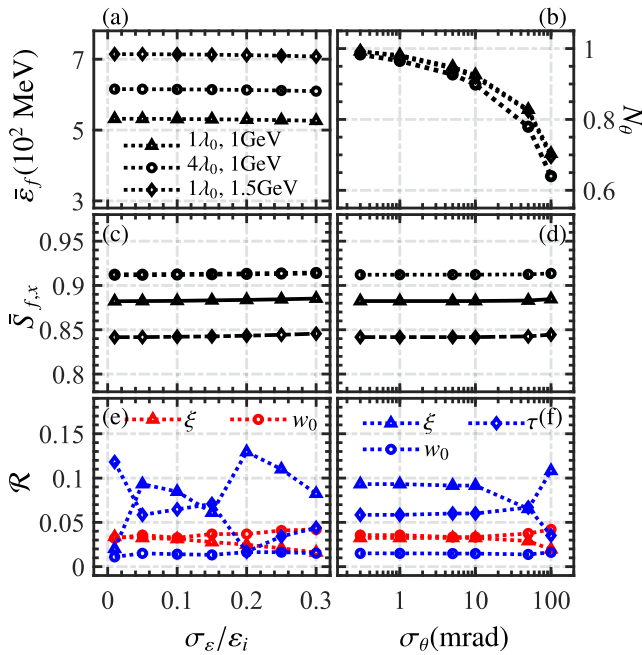


**FIG. 5.** Impact of probe electron beam parameters on detection signals. (a) Final average kinetic energies  $\bar{\varepsilon}_f$  vs initial energy spreads  $\sigma_\varepsilon/\varepsilon_i$  of probe electron beams ( $\sigma_\theta = 0.3$  mrad). Lines marked with triangles, circles, and diamonds denote probe electrons with different beam radii and energies. The initial spin polarization  $\bar{S}_{f,x} = 1$ , and the laser parameters are the same as in Fig. 4(d). (b) Relative changes in angular spread  $N_\theta = (\Delta\theta_{f,x} - \Delta\theta_{i,x})/\Delta\theta_{f,x}$  vs initial angular spread  $\sigma_\theta$  ( $\sigma_\varepsilon/\varepsilon_i = 0.05$ ) of probe electron beams, where  $\Delta\theta_{i,x}$  and  $\Delta\theta_{f,x}$  denote the full widths at half maximum (FWHM) of the initial and final angular spectra along the  $x$  direction, and  $\theta_x = \arctan(p_x/p_z)$ . (c) and (d) Final transverse spin degrees of polarization of scattered electron beams  $\bar{S}_{f,x}$  vs  $\sigma_\varepsilon/\varepsilon_i$  and  $\sigma_\theta$ , respectively. (e) and (f) Relative errors  $\mathcal{R}$  vs  $\sigma_\varepsilon/\varepsilon_i$  and  $\sigma_\theta$ , respectively. The red and blue lines are the relative errors  $\mathcal{R}$  of the analytical AE, for  $\xi$  and  $w_0$ , respectively. Lines marked with triangles, circles, and diamonds denote  $\mathcal{R}$  of  $\xi$ ,  $w_0$ , and  $\tau$ , respectively.

two orders of magnitude higher than that of the dynamic signal. The relative errors  $\mathcal{R}$  of the analytical AE and ML-assisted spin signals are shown in Figs. 5(e) and 5(f). Owing to angular and energy spread, the relative errors  $\mathcal{R}$  of the analytical AE, for  $\xi$  and  $w_0$ , are both kept within 5%, while the ML-assisted method can simultaneously predict three parameter values for  $\xi$ ,  $w_0$ , and  $\tau$ , with relative errors  $\mathcal{R} \lesssim 10\%$ . Especially for  $w_0$ , the accuracy of the ML-assisted method is at least twice as good as that of the analytical prediction.

#### IV. CONCLUSION

We have proposed an ML-assisted method to diagnose the spatiotemporal properties of an ultrafast ultraintense laser pulse, namely, the pulse duration  $\tau$ , peak intensity  $\xi$ , and focal spot size  $w_0$ , based on the radiative spin-flip effect of the electrons while they experience strong NCS. Our trained BPNN can accurately predict the spatiotemporal characteristics of petawatt-level laser systems with relative errors  $\lesssim 10\%$ . The proposed method is accurate and robust with respect to fluctuations in the electron beam parameters, and it is suitable for use with currently running or planned

multi-petawatt-scale laser facilities. Accurate measurement of ultrafast ultraintense laser parameters may pave the way for future strong-field experiments, of importance to laser nuclear physics investigations, laboratory astrophysics studies, and other fields.

#### ACKNOWLEDGMENTS

This work is supported by the National Natural Science Foundation of China (Grant Nos. 11874295, 12022506, U2267204, 11905169, 12275209, 11875219, and 12171383), the Open Fund of the State Key Laboratory of High Field Laser Physics (Shanghai Institute of Optics and Fine Mechanics), and the Foundation of Science and Technology on Plasma Physics Laboratory (Grant No. JCKYS2021212008). The work of Y.I.S. is supported by an American University of Sharjah Faculty Research (Grant No. FRG21).

#### AUTHOR DECLARATIONS

##### Conflict of Interest

The authors have no conflicts of interest to disclose.

#### Author Contributions

Zhi-Wei Lu and Xin-Di Hou contributed equally to this paper. Zhi-Wei Lu conducted the model building, simulation and paper writing, Xin-Di Hou constructed and optimized the neuron network, Feng Wan and Jian-Xing Li supervised the whole processes, Yousef I. Salamin discussed the results and improved the English-writing, Chong Lv and Bo Zhang discussed the experimental feasibility and revised the paper, Fei Wang instructed the neuron network building, Zhong-Feng Xu revised the paper.

**Zhi-Wei Lu:** Conceptualization (equal); Data curation (equal); Formal analysis (equal); Investigation (equal); Methodology (equal); Validation (equal); Visualization (equal); Writing – original draft (equal). **Xin-Di Hou:** Conceptualization (equal); Data curation (equal); Formal analysis (equal); Writing – original draft (equal). **Feng Wan:** Conceptualization (equal); Formal analysis (equal); Funding acquisition (equal); Project administration (equal); Supervision (equal); Writing – review & editing (equal). **Yousef I. Salamin:** Writing – review & editing (equal). **Chong Lv:** Formal analysis (equal); Writing – review & editing (equal). **Bo Zhang:** Writing – review & editing (equal). **Fei Wang:** Conceptualization (equal); Writing – review & editing (equal). **Zhong-Feng Xu:** Writing – review & editing (equal). **Jian-Xing Li:** Conceptualization (equal); Funding acquisition (equal); Investigation (equal); Project administration (equal); Software (equal); Supervision (equal); Writing – review & editing (equal).

#### DATA AVAILABILITY

The simulation data can be obtained from the authors.

#### REFERENCES

- S. Corde, K. Ta Phuoc, G. Lambert, R. Fitour, V. Malka, A. Rousse, A. Beck, and E. Lefebvre, “Femtosecond x rays from laser-plasma accelerators,” *Rev. Mod. Phys.* **85**, 1–48 (2013).

- <sup>2</sup>I. C. E. Turcu, F. Negoita, D. A. Jaroszynski, P. McKenna, S. Balascuta, D. Ursescu, I. Dancus, M. O. Cernaianu, M. V. Tataru, P. Ghenuche *et al.*, “High field physics and QED experiments at ELL-NP,” *Rom. Rep. Phys.* **68**, S145–S231 (2016).
- <sup>3</sup>E. Esarey, C. B. Schroeder, and W. P. Leemans, “Physics of laser-driven plasma-based electron accelerators,” *Rev. Mod. Phys.* **81**, 1229–1285 (2009).
- <sup>4</sup>A. Macchi, M. Borghesi, and M. Passoni, “Ion acceleration by superintense laser-plasma interaction,” *Rev. Mod. Phys.* **85**, 751–793 (2013).
- <sup>5</sup>B. Miao, J. E. Shrock, L. Feder, R. C. Hollinger, J. Morrison, R. Nedbailo, A. Picksley, H. Song, S. Wang, J. J. Rocca, and H. M. Milchberg, “Multi-GeV electron bunches from an all-optical laser wakefield accelerator,” *Phys. Rev. X* **12**, 031038 (2022).
- <sup>6</sup>R. Betti and O. A. Hurricane, “Inertial-confinement fusion with lasers,” *Nat. Phys.* **12**, 435–448 (2016).
- <sup>7</sup>J. Feng, W. Wang, C. Fu, L. Chen, J. Tan, Y. Li, J. Wang, Y. Li, G. Zhang, Y. Ma, and J. Zhang, “Femtosecond pumping of nuclear isomeric states by the coulomb collision of ions with quivering electrons,” *Phys. Rev. Lett.* **128**, 052501 (2022).
- <sup>8</sup>B. A. Remington, R. P. Drake, and D. D. Ryutov, “Experimental astrophysics with high power lasers and Z pinches,” *Rev. Mod. Phys.* **78**, 755–807 (2006).
- <sup>9</sup>S. V. Lebedev, A. Frank, and D. D. Ryutov, “Exploring astrophysics-relevant magnetohydrodynamics with pulsed-power laboratory facilities,” *Rev. Mod. Phys.* **91**, 025002 (2019).
- <sup>10</sup>A. Di Piazza, C. Müller, K. Z. Hatsagortsyan, and C. H. Keitel, “Extremely high-intensity laser interactions with fundamental quantum systems,” *Rev. Mod. Phys.* **84**, 1177–1228 (2012).
- <sup>11</sup>Z.-W. Lu, Q. Zhao, F. Wan, B.-C. Liu, Y.-S. Huang, Z.-F. Xu, and J.-X. Li, “Generation of arbitrarily polarized muon pairs via polarized  $e^-e^+$  collision,” *Phys. Rev. D* **105**, 113002 (2022).
- <sup>12</sup>J. W. Yoon, Y. G. Kim, I. W. Choi, J. H. Sung, H. W. Lee, S. K. Lee, and C. H. Nam, “Realization of laser intensity over  $10^{23}$  W/cm<sup>2</sup>,” *Optica* **8**, 630–635 (2021).
- <sup>13</sup>K. Poder, M. Tamburini, G. Sarri, A. Di Piazza, S. Kuschel, C. Baird, K. Behm, S. Bohlen, J. Cole, D. Corvan *et al.*, “Experimental signatures of the quantum nature of radiation reaction in the field of an ultraintense laser,” *Phys. Rev. X* **8**, 031004 (2018).
- <sup>14</sup>J. M. Cole, K. T. Behm, E. Gerstmayr, T. G. Blackburn, J. C. Wood, C. D. Baird, M. J. Duff, C. Harvey, A. Ilderton, A. S. Joglekar *et al.*, “Experimental evidence of radiation reaction in the collision of a high-intensity laser pulse with a laser-wakefield accelerated electron beam,” *Phys. Rev. X* **8**, 011020 (2018).
- <sup>15</sup>M. Tabak, J. Hammer, M. E. Glinisky, W. L. Krueer, S. C. Wilks, J. Woodworth, E. M. Campbell, M. D. Perry, and R. J. Mason, “Ignition and high gain with ultrapowerful lasers,” *Phys. Plasmas* **1**, 1626–1634 (1994).
- <sup>16</sup>J. Fuchs, P. Anticci, E. d’Humières, E. Lefebvre, M. Borghesi, E. Brambrink, C. A. Cecchetti, M. Kaluza, V. Malka, M. Manclossi *et al.*, “Laser-driven proton scaling laws and new paths towards energy increase,” *Nat. Phys.* **2**, 48–54 (2006).
- <sup>17</sup>T. Bartal, M. E. Foord, C. Bellei, M. H. Key, K. A. Flippo, S. A. Gaillard, D. T. Offermann, P. K. Patel, L. C. Jarrott, D. P. Higginson *et al.*, “Focusing of short-pulse high-intensity laser-accelerated proton beams,” *Nat. Phys.* **8**, 139–142 (2012).
- <sup>18</sup>R. A. Simpson, G. G. Scott, D. Mariscal, D. Rusby, P. M. King, E. Grace, A. Aghedo, I. Pagano, M. Sinclair, C. Armstrong *et al.*, “Scaling of laser-driven electron and proton acceleration as a function of laser pulse duration, energy, and intensity in the multi-picosecond regime,” *Phys. Plasmas* **28**, 013108 (2021).
- <sup>19</sup>R. Trebino, R. Jafari, S. A. Akturk, P. Bowlan, Z. Guang, P. Zhu, E. Escoto, and G. Steinmeyer, “Highly reliable measurement of ultrashort laser pulses,” *J. Appl. Phys.* **128**, 171103 (2020).
- <sup>20</sup>O. E. Vais, A. G. R. Thomas, A. M. Maksimchuk, K. Krushelnick, and V. Y. Bychenkov, “Characterizing extreme laser intensities by ponderomotive acceleration of protons from rarified gas,” *New J. Phys.* **22**, 023003 (2020).
- <sup>21</sup>M. F. Ciappina, E. E. Paganov, and S. V. Popruzhenko, “Focal-shape effects on the efficiency of the tunnel-ionization probe for extreme laser intensities,” *Matter Radiat. Extremes* **5**, 044401 (2020).
- <sup>22</sup>C. N. Harvey, “*In situ* characterization of ultraintense laser pulses,” *Phys. Rev. Accel. Beams* **21**, 114001 (2018).
- <sup>23</sup>G. Pretzler, A. Kasper, and K. J. Witte, “Angular chirp and tilted light pulses in CPA lasers,” *Appl. Phys. B* **70**, 1–9 (2000).
- <sup>24</sup>G. Pariente, V. Gallet, A. Borot, O. Gobert, and F. Quéré, “Space-time characterization of ultra-intense femtosecond laser beams,” *Nat. Photonics* **10**, 547–553 (2016).
- <sup>25</sup>Z. Li, K. Tsubakimoto, H. Yoshida, Y. Nakata, and N. Miyanaga, “Degradation of femtosecond petawatt laser beams: Spatio-temporal/spectral coupling induced by wavefront errors of compression gratings,” *Appl. Phys. Express* **10**, 102702 (2017).
- <sup>26</sup>M. F. Ciappina, S. V. Popruzhenko, S. V. Bulanov, T. Ditmire, G. Korn, and S. Weber, “Progress toward atomic diagnostics of ultrahigh laser intensities,” *Phys. Rev. A* **99**, 043405 (2019).
- <sup>27</sup>M. F. Ciappina and S. V. Popruzhenko, “Diagnostics of ultra-intense laser pulses using tunneling ionization,” *Laser Phys. Lett.* **17**, 025301 (2020).
- <sup>28</sup>K. A. Ivanov, I. N. Tymbalov, O. E. Vais, S. G. Bochkarev, R. V. Volkov, V. Y. Bychenkov, and A. B. Savel’ev, “Accelerated electrons for in situ peak intensity monitoring of tightly focused femtosecond laser radiation at high intensities,” *Plasma Phys. Controlled Fusion* **60**, 105011 (2018).
- <sup>29</sup>O. E. Vais and V. Yu. Bychenkov, “Direct electron acceleration for diagnostics of a laser pulse focused by an off-axis parabolic mirror,” *Appl. Phys. B* **124**, 211 (2018).
- <sup>30</sup>K. Krajewska, F. Cajiao Vélez, and J. Z. Kamiński, “High-energy ionization for intense laser pulse diagnostics,” *Plasma Phys. Controlled Fusion* **61**, 074004 (2019).
- <sup>31</sup>O. E. Vais and V. Yu. Bychenkov, “Complementary diagnostics of high-intensity femtosecond laser pulses via vacuum acceleration of protons and electrons,” *Plasma Phys. Controlled Fusion* **63**, 014002 (2020).
- <sup>32</sup>J.-X. Li, Y.-Y. Chen, K. Z. Hatsagortsyan, and C. H. Keitel, “Single-shot carrier-envelope phase determination of long superintense laser pulses,” *Phys. Rev. Lett.* **120**, 124803 (2018).
- <sup>33</sup>F. Mackenroth, A. R. Holkundkar, and H.-P. Schlenvoigt, “Ultra-intense laser pulse characterization using ponderomotive electron scattering,” *New J. Phys.* **21**, 123028 (2019).
- <sup>34</sup>O. Har-Shemesh and A. Di Piazza, “Peak intensity measurement of relativistic lasers via nonlinear Thomson scattering,” *Opt. Lett.* **37**, 1352–1354 (2012).
- <sup>35</sup>C. Z. He, A. Longman, J. A. Pérez-Hernández, M. de Marco, C. Salgado, G. Zeraoui, G. Gatti, L. Roso, R. Fedosejevs, and W. T. Hill, “Towards an *in situ*, full-power gauge of the focal-volume intensity of petawatt-class lasers,” *Opt. Express* **27**, 30020–30030 (2019).
- <sup>36</sup>F. Mackenroth and A. R. Holkundkar, “Determining the duration of an ultra-intense laser pulse directly in its focus,” *Sci. Rep.* **9**, 19607–19612 (2019).
- <sup>37</sup>I. A. Aleksandrov and A. A. Andreev, “Pair production seeded by electrons in noble gases as a method for laser intensity diagnostics,” *Phys. Rev. A* **104**, 052801 (2021).
- <sup>38</sup>Y.-F. Li, R. Shaisultanov, K. Z. Hatsagortsyan, F. Wan, C. H. Keitel, and J.-X. Li, “Ultrarelativistic electron-beam polarization in single-shot interaction with an ultraintense laser pulse,” *Phys. Rev. Lett.* **122**, 154801 (2019).
- <sup>39</sup>H.-H. Song, W.-M. Wang, J.-X. Li, Y.-F. Li, and Y.-T. Li, “Spin-polarization effects of an ultrarelativistic electron beam in an ultraintense two-color laser pulse,” *Phys. Rev. A* **100**, 033407 (2019).
- <sup>40</sup>Y. F. Li, R. Shaisultanov, Y. Y. Chen, F. Wan, K. Z. Hatsagortsyan, C. H. Keitel, and J. X. Li, “Polarized ultrashort brilliant multi-GeV  $\gamma$  rays via single-shot laser-electron interaction,” *Phys. Rev. Lett.* **124**, 014801 (2020).
- <sup>41</sup>G. Karagiorgi, G. Kasieczka, S. Kravitz, B. Nachman, and D. Shih, “Machine learning in the search for new fundamental physics,” *Nat. Rev. Phys.* **4**, 399–412 (2022).
- <sup>42</sup>J. VanderPlas, A. J. Connolly, Ž. Ivezić, and A. Gray, “Introduction to astroML: Machine learning for astrophysics,” in *2012 Conference on Intelligent Data Understanding* (IEEE, 2012), pp. 47–54.
- <sup>43</sup>G. Carleo, I. Cirac, K. Cranmer, L. Daudet, M. Schuld, N. Tishby, L. Vogt-Maranto, and L. Zdeborová, “Machine learning and the physical sciences,” *Rev. Mod. Phys.* **91**, 045002 (2019).
- <sup>44</sup>G. R. Schleder, A. C. M. Padilha, C. M. Acosta, M. Costa, and A. Fazzio, “From DFT to machine learning: Recent approaches to materials science—a review,” *J. Phys. Mater.* **2**, 032001 (2019).
- <sup>45</sup>J. Carrasquilla, “Machine learning for quantum matter,” *Adv. Phys.: X* **5**, 1797528 (2020).



- <sup>46</sup>M. Raghu and E. Schmidt, "A survey of deep learning for scientific discovery," [arXiv:2003.11755](https://arxiv.org/abs/2003.11755) (2020).
- <sup>47</sup>M. E. Martin, R. A. London, S. Goluoglu, and H. D. Whitley, "An automated design process for short pulse laser driven opacity experiments," *High Energy Density Phys.* **26**, 26–37 (2018).
- <sup>48</sup>P. W. Hatfield, S. J. Rose, and R. H. H. Scott, "The blind implosion-maker: Automated inertial confinement fusion experiment design," *Phys. Plasmas* **26**, 062706 (2019).
- <sup>49</sup>P. W. Hatfield, J. A. Gaffney, G. J. Anderson, S. Ali, L. Antonelli, S. Başeğmez du Pree, J. Citrin, M. Fajardo, P. Knapp, B. Kettle *et al.*, "The data-driven future of high-energy-density physics," *Nature* **593**, 351–361 (2021).
- <sup>50</sup>J. Biener, D. D. Ho, C. Wild, E. Woerner, M. M. Biener, B. S. El-Dasher, D. G. Hicks, J. H. Eggert, P. M. Celliers, G. W. Collins *et al.*, "Diamond spheres for inertial confinement fusion," *Nucl. Fusion* **49**, 112001 (2009).
- <sup>51</sup>M. J. MacDonald, T. Gorkhover, B. Bachmann, M. Bucher, S. Carron, R. N. Coffee, R. P. Drake, K. R. Ferguson, L. B. Fletcher, E. J. Gamboa *et al.*, "Measurement of high-dynamic range x-ray Thomson scattering spectra for the characterization of nano-plasmas at LCLS," *Rev. Sci. Instrum.* **87**, 11E709 (2016).
- <sup>52</sup>M. Wen, M. Tamburini, and C. H. Keitel, "Polarized laser-wakefield-accelerated kiloampere electron beams," *Phys. Rev. Lett.* **122**, 214801 (2019).
- <sup>53</sup>Z. Nie, F. Li, F. Morales, S. Patchkovskii, O. Smirnova, W. An, N. Nambu, D. Matteo, K. A. Marsh, F. Tsung *et al.*, "In situ generation of high-energy spin-polarized electrons in a beam-driven plasma wakefield accelerator," *Phys. Rev. Lett.* **126**, 054801 (2021).
- <sup>54</sup>D. Seipt, D. Del Sorbo, C. P. Ridgers, and A. G. R. Thomas, "Ultrafast polarization of an electron beam in an intense bichromatic laser field," *Phys. Rev. A* **100**, 061402 (2019).
- <sup>55</sup>K. Xue, R.-T. Guo, F. Wan, R. Shaisultanov, Y.-Y. Chen, Z.-F. Xu, X.-G. Ren, K. Z. Hatsagortsyan, C. H. Keitel, and J.-X. Li, "Generation of arbitrarily polarized GeV lepton beams via nonlinear Breit-Wheeler process," *Fundam. Res.* **2**, 539–545 (2022).
- <sup>56</sup>N. F. Mott, "The scattering of fast electrons by atomic nuclei," *Proc. R. Soc. London A* **124**, 425–442 (1929).
- <sup>57</sup>P. S. Cooper, M. J. Alguard, R. D. Ehrlich, V. W. Hughes, H. Kobayakawa, J. S. Ladish, M. S. Lubell, N. Sasao, K. P. Schuler, P. A. Souder, G. Baum, W. Raith, K. Kondo, D. H. Coward, R. H. Miller, C. Y. Prescott, D. J. Sherden, and C. K. Sinclair, "Polarized electron-electron scattering at GeV energies," *Phys. Rev. Lett.* **34**, 1589–1592 (1975).
- <sup>58</sup>O. Klein and Y. Nishina, "Über die Streuung von Strahlung durch freie Elektronen nach der neuen relativistischen Quantendynamik von Dirac," *Z. Phys.* **52**, 853–868 (1929).
- <sup>59</sup>Y.-F. Li, R.-T. Guo, R. Shaisultanov, K. Z. Hatsagortsyan, and J.-X. Li, "Electron polarimetry with nonlinear Compton scattering," *Phys. Rev. Appl.* **12**, 014047 (2019).
- <sup>60</sup>K. Xue, Z.-K. Dou, F. Wan, T.-P. Yu, W.-M. Wang, J.-R. Ren, Q. Zhao, Y.-T. Zhao, Z.-F. Xu, and J.-X. Li, "Generation of highly-polarized high-energy brilliant  $\gamma$ -rays via laser-plasma interaction," *Matter Radiat. Extremes* **5**, 054402 (2020).
- <sup>61</sup>V. Katkov, V. M. Strakhovenko *et al.*, *Electromagnetic Processes at High Energies in Oriented Single Crystals* (World Scientific, 1998).
- <sup>62</sup>V. I. Ritus, "Quantum effects of the interaction of elementary particles with an intense electromagnetic field," *J. Sov. Laser Res.* **6**, 497 (1985).
- <sup>63</sup>A. Paszke, S. Gross, F. Massa, A. Lerer, J. Bradbury, G. Chanan, T. Killeen, Z. Lin, N. Gimelshein, L. Antiga, "PyTorch: An imperative style, high-performance deep learning library," in *Proceedings of the 33rd International Conference on Neural Information Processing Systems* (Curran Associates Inc., 2019), article no. 721.
- <sup>64</sup>N. Srebro and A. Shraibman, "Rank, trace-norm and max-norm," in *International Conference on Computational Learning Theory* (Springer, 2005), pp. 545–560.
- <sup>65</sup>N. Srivastava, G. Hinton, A. Krizhevsky, I. Sutskever, and R. Salakhutdinov, "Dropout: A simple way to prevent neural networks from overfitting," *J. Mach. Learn. Res.* **15**, 1929–1958 (2014).
- <sup>66</sup>L. D. Landau and E. M. Lifshitz, *The Classical Theory of Fields*, Course of theoretical physics (Pergamon Press Ltd., 1975). Vol. 2.
- <sup>67</sup>R.-T. Guo, Y. Wang, R. Shaisultanov, F. Wan, Z.-F. Xu, Y.-Y. Chen, K. Z. Hatsagortsyan, and J.-X. Li, "Stochasticity in radiative polarization of ultra-relativistic electrons in an ultrastrong laser pulse," *Phys. Rev. Res.* **2**, 033483 (2020).
- <sup>68</sup>F. Niel, C. Riconda, F. Amiranoff, R. Ducloux, and M. Grech, "From quantum to classical modeling of radiation reaction: A focus on stochasticity effects," *Phys. Rev. E* **97**, 043209 (2018).
- <sup>69</sup>M. Tamburini, F. Pegoraro, A. Di Piazza, C. H. Keitel, and A. Macchi, "Radiation reaction effects on radiation pressure acceleration," *New J. Phys.* **12**, 123005 (2010).
- <sup>70</sup>K. A. Tanaka, K. M. Spohr, D. L. Balabanski, S. Balascuta, L. Capponi, M. O. Cernaianu, M. Cuciu, A. Cucoanes, I. Dancus, A. Dhal *et al.*, "Current status and highlights of the ELI-NP research program," *Matter Radiat. Extremes* **5**, 024402 (2020).
- <sup>71</sup>M. Aoyama, K. Yamakawa, Y. Akahane, J. Ma, N. Inoue, H. Ueda, and H. Kiriya, "0.85-PW, 33-fs Ti: Sapphire laser," *Opt. Lett.* **28**, 1594–1596 (2003).
- <sup>72</sup>T. J. Yu, S. K. Lee, J. H. Sung, J. W. Yoon, T. M. Jeong, and J. Lee, "Generation of high-contrast, 30 fs, 1.5 PW laser pulses from chirped-pulse amplification Ti: Sapphire laser," *Opt. Express* **20**, 10807–10815 (2012).
- <sup>73</sup>W. Hong, S. He, J. Teng, Z. Deng, Z. Zhang, F. Lu, B. Zhang, B. Zhu, Z. Dai, B. Cui *et al.*, "Commissioning experiment of the high-contrast SILEX-II multi-petawatt laser facility," *Matter Radiat. Extremes* **6**, 064401 (2021).
- <sup>74</sup>K. Burdonov, A. Fazzini, V. Lelasseux, J. Albrecht, P. Antici, Y. Ayoul, A. Beluze, D. Cavanna, T. Ceccotti, M. Chabanis *et al.*, "Characterization and performance of the Apollon short-focal-area facility following its commissioning at 1 PW level," *Matter Radiat. Extremes* **6**, 064402 (2021).